

Ceramic–Salt Composite Electrolytes from Cold Sintering

Wonho Lee, Christopher K. Lyon, Joo-Hwan Seo, Raymond Lopez-Hallman, Yongjun Leng, Chao-Yang Wang, Michael A. Hickner, Clive A. Randall, and Enrique D. Gomez*

The development of solid electrolytes with the combination of high ionic conductivity, electrochemical stability, and resistance to Li dendrites continues to be a challenge. A promising approach is to create inorganic–organic composites, where multiple components provide the needed properties, but the high sintering temperature of materials such as ceramics precludes close integration or co-sintering. Here, new ceramic–salt composite electrolytes that are cold sintered at 130 °C are demonstrated. As a model system, composites of $\text{Li}_{1.5}\text{Al}_{0.5}\text{Ge}_{1.5}(\text{PO}_4)_3$ (LAGP) or $\text{Li}_{1+x}\text{Al}_x\text{Ti}_{2-x}\text{Si}_y\text{P}_{3-y}\text{O}_{12}$ (LATP) with bis(trifluoromethanesulfonyl)imide (LiTFSI) salts are cold sintered. The resulting LAGP–LiTFSI and LATP–LiTFSI composites exhibit high relative densities of about 90% and ionic conductivities in excess of $10^{-4} \text{ S cm}^{-1}$ at 20 °C, which are comparable with the values obtained from LAGP and LATP sintered above 800 °C. It is also demonstrated that cold sintered LAGP–LiTFSI is electrochemically stable in Li symmetric cells over 1800 h at 0.2 mAh cm^{-2} . Cold sintering provides a new approach for bridging the gap in processing temperatures of different materials, thereby enabling high-performance composites for electrochemical systems.

electrode), low density (0.53 g cm^{-3}), and a theoretical capacity of 3860 mAh g^{-1} are poised to meet the needs of next-generation energy storage.^[2–4] Nevertheless, current Li metal batteries that use combinations of organic liquid and salt as electrolytes suffer from rapid capacity fade upon cycling.^[5–7] Li metal anodes lead to inhomogeneous and unstable solid electrolyte interphases (SEIs), promote dendrite growth that short the cell, consume electrolyte during cycling, and create potential problems with flammability and explosions.^[5–7]

Ceramic-based solid electrolytes are a promising class of materials that enable safer Li metal batteries because they are nonflammable and have a large range of electrochemical stability.^[4,8] Furthermore, ceramic electrolytes have Li transference numbers of unity and high elastic moduli compared to polymeric electrolytes, which may be crucial to suppress dendrite growth.^[5]

Among various ceramic solid electrolytes,^[4,8–14] sodium super ionic conductor (NASICON)-type oxide electrolytes have been highlighted as promising candidates because they exhibit ionic conductivities near $10^{-4} \text{ S cm}^{-1}$ at room temperature and good chemical stability against water and air.^[4,8,11–14] Nevertheless, sintering of these oxide electrolytes requires high temperature, above 800 °C, to achieve high densities and high ionic conductivities.^[9,12,14–17] Such a sintering process has obvious limitations, including Li loss, impurity phase formation, incompatibility with organic materials, difficulties in integrating all-solid-state batteries with composite cathodes, and high processing cost.^[18,19]

A recently developed approach, cold sintering, can densify ceramics near 100 °C by incorporating a transient solvent phase and uniaxial pressure into the process.^[18,20–23] As a consequence, ceramics such as alkali molybdates, BaTiO_3 , and $\text{Li}_{1.5}\text{Al}_{0.5}\text{Ge}_{1.5}(\text{PO}_4)_3$ (LAGP) can be sintered at a temperature that is an order of magnitude lower than through conventional means.^[18,23] Furthermore, the low processing temperature of cold sintering enables co-sintering of ceramics with polymers, for applications in microwave dielectrics (Li_2MoO_4 /polytetrafluoroethylene), semiconductors (V_2O_4 /poly(3,4-ethylenedioxythiophene)-poly(styrenesulfonate)), and solid electrolytes (LAGP/poly(vinylidene fluoride-co-hexafluoropropylene)).^[21] Although densification of LAGP and LAGP composites is achieved at 120 °C to densities of 85% using water as a transient solvent, cold sintered solid electrolytes have low

1. Introduction

Li-ion batteries have been successfully commercialized due to their long cycle life and high charge/discharge rate, but their energy densities with conventional graphitic anodes are insufficient for emerging applications, such as electric vehicles, grid-level energy storage, and personal electronic devices.^[1,2] As such, Li metal anodes that have the lowest known electrochemical potential (-3.04 V vs the standard hydrogen

Dr. W. Lee,^[†] Dr. C. K. Lyon, Prof. E. D. Gomez
Department of Chemical Engineering
The Pennsylvania State University
University Park, PA 16802, USA
E-mail: edg12@psu.edu

J.-H. Seo, R. Lopez-Hallman, Prof. M. A. Hickner, Prof. C. A. Randall
Department of Materials Science and Engineering
The Pennsylvania State University
University Park, PA 16802, USA

Dr. Y. Leng, Prof. C.-Y. Wang
Department of Mechanical and Nuclear Engineering
The Pennsylvania State University
University Park, PA 16802, USA

 The ORCID identification number(s) for the author(s) of this article can be found under <https://doi.org/10.1002/adfm.201807872>.

^[†]Present address: Department of Polymer Science and Engineering, Kumoh National Institute of Technology, Gumi, Gyeongbuk 39177, Korea

DOI: 10.1002/adfm.201807872

ionic conductivities of about 10^{-6} S cm^{-1} at room temperature.^[18] Given that cold sintered electrolytes show the same crystal structure within grains, it is speculated that a key challenge lies in amorphous, low-conductivity grain boundaries that may be a result of incongruent dissolution in water of the constituent elements.^[18,23]

Here, we propose an approach to synthesize ceramic–salt composite electrolytes to mitigate the inherent high grain boundary resistances that result from cold sintering. We introduce bis(trifluoromethanesulfonyl)imide lithium (LiTFSI) salt in aqueous solutions as a cold sintering solvent for LAGP and $\text{Li}_{1+x+y}\text{Al}_x\text{Ti}_{2-x}\text{Si}_y\text{P}_{3-y}\text{O}_{12}$ (LATP). Cold sintering of LAGP or LATP at 130 °C with LiTFSI (CS LAGP–LiTFSI and CS LATP–LiTFSI) leads to relative densities near 90% and conductivities around 10^{-4} S cm^{-1} at 20 °C. Conductivities and activation energies of cold sintered composites are almost identical to conductivities of LAGP and LATP that were sintered above 800 °C (S LAGP and S LATP). We also demonstrate that CS LAGP–LiTFSI can be cycled in Li symmetric cells over 1800 h at 0.2 mAh cm^{-2} .

2. Results and Discussion

Cold sintering of ceramic electrolytes requires the application of a small amount of solvent, high pressure, and modest temperatures to leverage a dissolution–precipitation process that reduces sintering temperatures to less than 200 °C;^[20] nevertheless, this process can lead to amorphous grain boundaries that are detrimental to ionic conduction.^[18,23] We thus propose that the addition of a second phase, such as a Li salt, can reduce grain boundary resistances. LiTFSI was chosen to demonstrate the concept of ceramic–salt composite electrolytes through cold sintering because LiTFSI is highly soluble in water and stable against hydrolysis, and has a high decomposition temperature above 300 °C.^[24] The salt was introduced through dissolution in the cold sintering solvent as shown in **Figure 1**. Subsequent application of pressure and heat leads to cold sintered LAGP or LATP composites, CS LAGP–LiTFSI and CS LATP–LiTFSI. We optimized cold sintering conditions by varying the uniaxial pressure to obtain densified electrolytes. We found that relative densities of CS LAGP and CS LATP gradually increase with increasing pressures, where CS LAGP and CS LATP show the highest relative densities under 380 and 620 MPa at 130 °C,

respectively (Figure S1, Supporting Information). To examine the effect of LiTFSI on Li-ion transport and sinterability, we varied volume fractions of LiTFSI relative to LAGP and LATP in the range of 0–21% by volume. Preparation details are found in the “Experimental Section.”

Figure 2a and Table S1 (Supporting Information) show relative densities and total ionic conductivities (σ) of CS LAGP–LiTFSI containing different vol% of LiTFSI. Conductivities are obtained from Nyquist plots of symmetric cells (Au/electrolyte/Au) at 20 °C (Figure S2, Supporting Information). Adding a small amount of LiTFSI (4.0 vol%) significantly increases the ionic conductivity, leading to an order of magnitude increase from 7.6×10^{-6} S cm^{-1} (CS LAGP) to 7.7×10^{-5} S cm^{-1} (CS LAGP–LiTFSI 4.0 vol%) (Figure 2a; Table S1, Supporting Information). Increasing the LiTFSI content further continues to increase ionic conductivities, with a maximum value of 2.3×10^{-4} S cm^{-1} at 17 vol% LiTFSI. Relative densities are constant (87–89%) for all LiTFSI compositions, indicating that the salt did not have an adverse effect on densification. The Young’s modulus (E) of cold sintered electrolytes was measured through nanoindentation. As shown in Figure S3 (Supporting Information), E of CS LAGP was 200 GPa, near that of other reported values for ceramic electrolytes,^[25] while that of CS LAGP–LiTFSI was 140 GPa. Moduli of both CS LAGP and CS LAGP–LiTFSI are significantly higher than Li metal, suggesting the potential to stop dendrite growth in lithium cells.

We also show cold sintering of ceramic–salt composite electrolytes using another NASICON-type electrolyte, LATP. The LATP powder used was a glass-ceramic ($\text{Li}_{1+x+y}\text{Al}_x\text{Ti}_{2-x}\text{Si}_y\text{P}_{3-y}\text{O}_{12}$, Ohara), which has higher ionic conductivities and better mechanical properties than that of pure LATP (see the Experimental Section).^[26,27] As shown in Figure 2b, a similar trend is observed as in CS LAGP–LiTFSI, where a high ionic conductivity was obtained from 17 vol% LiTFSI in CS LATP–LiTFSI. Thus, conductivities of about 10^{-4} S cm^{-1} obtained from 17 vol% LiTFSI in CS LAGP–LiTFSI and CS LATP–LiTFSI composite electrolytes are similar to values obtained from LAGP and LATP sintered above 800 °C (S LAGP and S LATP) (Table S1, Supporting Information). Although LiTFSI significantly enhances ionic conductivities, ion transport through the ceramic phase is important; replacing the ceramic ion conductor with an insulator $\text{Na}_2\text{Mo}_2\text{O}_7$ leads to poor ionic conductivities of 10^{-7} S cm^{-1} , even with

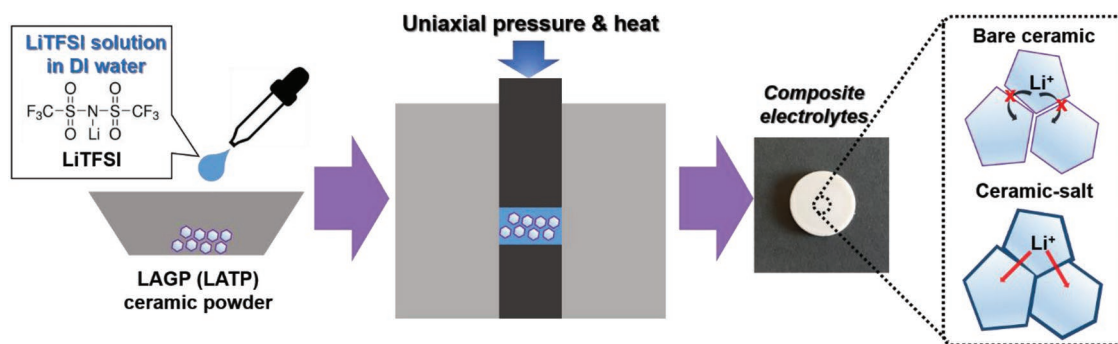


Figure 1. Schematic illustration of cold sintering to produce composite electrolytes comprised of ceramics and organic Li salts. Processing temperature of 130 °C.

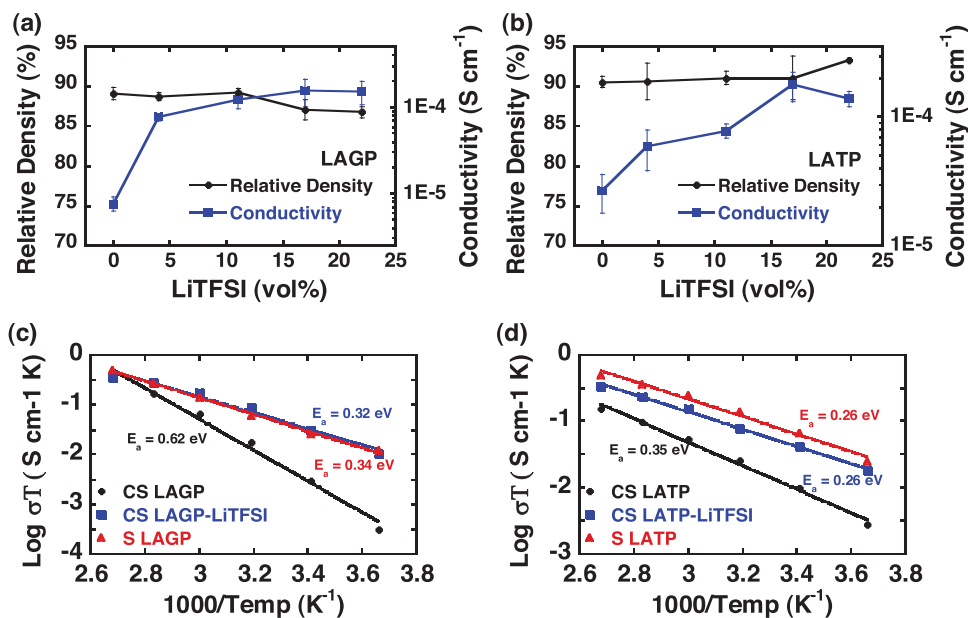


Figure 2. Relative density and ionic conductivity at 20 °C of a) CS LAGP–LiTFSI and b) CS LAMP–LiTFSI composite electrolytes with different LiTFSI contents. Relative densities calculated from theoretical maximum (LAGP) or from a conventionally sintered film as reference (LAMP). Temperature dependence of ionic conductivity for c) CS LAGP–LiTFSI and d) CS LAMP–LiTFSI; for comparison, data from S LAGP and S LAMP are also included.

excess amount of LiTFSI (30 vol%) (Figure S4, Supporting Information).

Figure 2c shows the temperature dependence of the ionic conductivity of CS LAGP, CS LAGP–LiTFSI (17 vol% LiTFSI), and S LAGP in the range of 0–100 °C. All electrolytes exhibit Arrhenius behavior as expected.^[12] The activation energy E_a from S LAGP was 0.34 eV, which is similar to values from previous reports.^[12,28] CS LAGP–LiTFSI has a similar E_a of 0.32 eV, although E_a of CS LAGP is much higher (0.62 eV). We attribute the higher activation energy of CS LAGP to the amorphous grain boundaries that result from incongruent dissolution in water of the constituent elements,^[18,23] and the enhanced conductivities of CS LAGP–LiTFSI to reduced grain boundary resistances. Indeed, we find a significantly reduced grain boundary resistance in CS LAGP–LiTFSI when compared to CS LAGP, as determined from Nyquist plots taken at low temperatures (–20 °C) to distinguish resistances of grain boundaries from grains using an equivalent circuit model (Figure S5, Supporting Information). Conductivities of grain boundaries of CS LAGP–LiTFSI ($\sigma_{gb} = 4.1 \times 10^{-5} \text{ S cm}^{-1}$) were two orders of magnitude higher than that of CS LAGP ($\sigma_{gb} = 3.4 \times 10^{-7} \text{ S cm}^{-1}$), while both electrolytes showed similar grain conductivities on the order of $10^{-5} \text{ S cm}^{-1}$.

CS LAMP–LiTFSI has an E_a of 0.26 eV that is also the same as that of S LAMP (0.26 eV), but is lower than that of CS LAMP (0.35 eV). E_a values of CS LAMP–LiTFSI and S LAMP were slightly lower than previously reported for LAMP, which ranged from 0.3 to 0.4 eV, likely due to a different composition of LAMP.^[29] We thus conclude that cold sintering of ceramic–salt electrolytes can effectively densify composites and leads to high ionic conductivities despite the remarkably low processing temperatures.

The densified microstructure of ceramic–salt composite electrolytes was imaged using scanning electron microscopy (SEM),

as shown in Figure 3a. Cold sintering of LAGP clearly produces densely packed microstructures without any observable pores. In addition, no grain growth is apparent, similarly to previous work.^[20] CS LAGP–LiTFSI shows nearly identical microstructures with CS LAGP. Densely packed microstructures through cold sintering are also apparent in CS LAMP and CS LAMP–LiTFSI, as shown in Figure 3b. Grains are not as apparent in CS LAMP–LiTFSI, perhaps due to the amorphous glass phase of the LAMP powder used for cold sintering.^[27]

The crystal structures of LAGP, LAMP, and composites with LiTFSI were examined using X-ray diffraction (XRD) (Figure 4). XRD patterns of LAGP powder, CS LAGP, and CS LAGP–LiTFSI are shown in Figure 4a. The main phase of LAGP powder is a NASICON-type hexagonal crystal structure, $\text{Li}[\text{Ge}(\text{PO}_4)_3]$.^[15,28] Two impurity phases of GeO_2 ($q \approx 1.84 \text{ \AA}^{-1}$) and AlPO_4 ($q \approx 1.87 \text{ \AA}^{-1}$) in small amounts are also present (Figure S6, Supporting Information). Unit cell parameters of hexagonal structures and amounts of impurity phases are summarized in Table 1. Cold sintering preserves the hexagonal structures of LAGP; no additional peaks are apparent, and unit cell parameters for LAGP powder, CS LAGP, and CS LAGP–LiTFSI are essentially invariant (Table 1). The impurity GeO_2 was nearly unperturbed, but the amount of AlPO_4 was slightly increased from 5.3 to 8.4 wt% after cold sintering. Results of cold sintered LAMP are similar; the NASICON-type hexagonal crystal structure is preserved, and the amount of an impurity phase (TiO_2 , $q \approx 1.94 \text{ \AA}^{-1}$) is almost the same before and after cold sintering (Figure S6, Supporting Information). Nevertheless, the AlPO_4 phase appears after the cold sintering process. Although cold sintering of LAGP or LAMP induces the formation of an AlPO_4 phase, the amount is 2% or less of the total sample. Thus, cold sintering ceramic powders at low temperatures ($\approx 130 \text{ °C}$) in the presence of LiTFSI do not significantly affect the crystal structure of LAGP or LAMP.

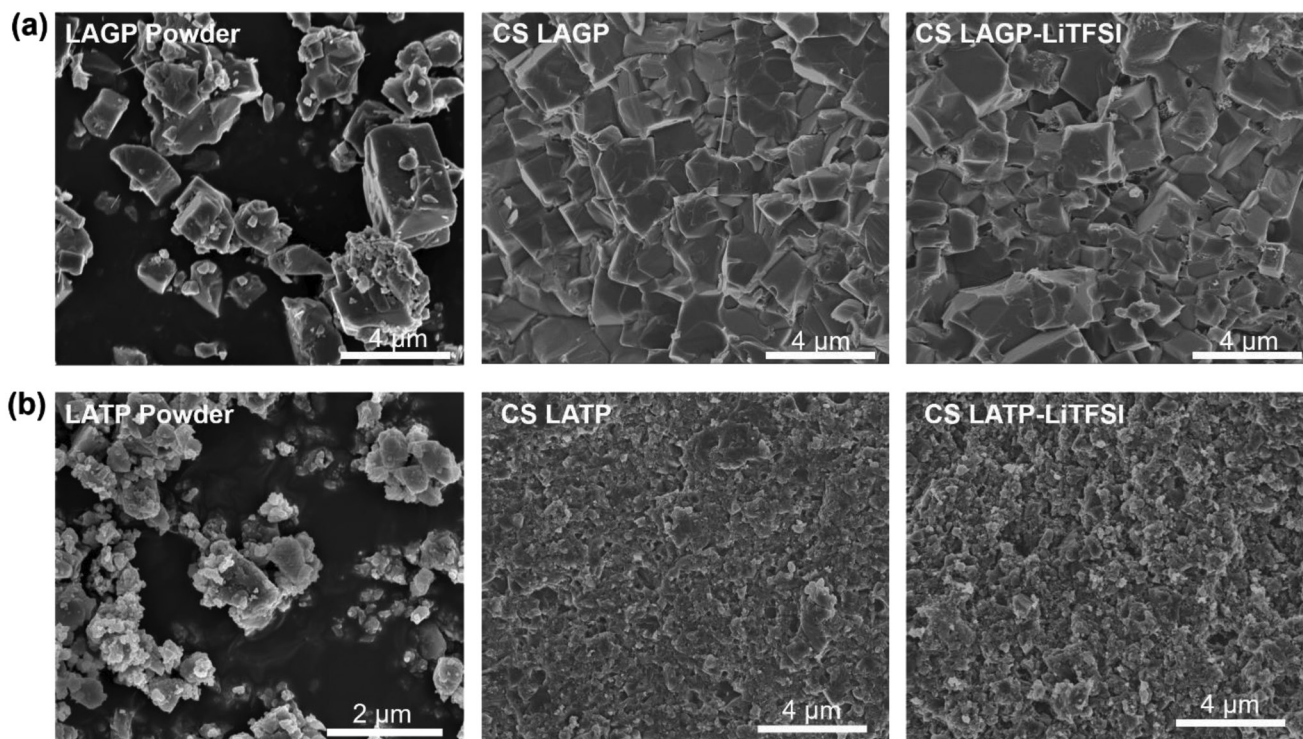


Figure 3. SEM images of fracture surfaces of a) LAGP and b) LATP composite electrolytes. In the case of CS LAGP–LiTFSI and CS LATP–LiTFSI, 17 vol% LiTFSI was incorporated.

We can also examine the local environment within LAGP and of LiTFSI using Fourier-transform infrared spectroscopy (FT-IR). As shown in Figure S7 (Supporting Information), both CS LAGP and CS LAGP–LiTFSI exhibit predominant absorption bands in the 900–1300 cm^{-1} region that corresponds to the asymmetric stretch of the PO_4^{3-} ionic group of LAGP.^[30] Absorption bands in CS LAGP–LiTFSI were observed at 720–820 cm^{-1} , $\approx 1200 \text{ cm}^{-1}$, and 1300–1400 cm^{-1} . These correspond to the characteristic peaks of LiTFSI.^[31]

In order to reveal shifts associated with the local environment of LiTFSI in the presence of water, we examined the FT-IR spectra of LiTFSI in deionized (DI) water at concentrations from 1 M (dilute solution) to 22 M (saturated solution). **Figure 5** compares the peak shift of the symmetric stretch of sulfur-nitrogen-sulfur (SNS) groups ($\nu_{(s)}\text{SNS}$) (Figure 5a), the asymmetric stretch of SNS ($\nu_{(as)}\text{SNS}$) (Figure 5b), and in-plane symmetric deformation of CF_3 groups ($\delta_{(s)}\text{CF}_3$) (Figure 5c). Upon dissolving LiTFSI in DI water (1 M concentration), the

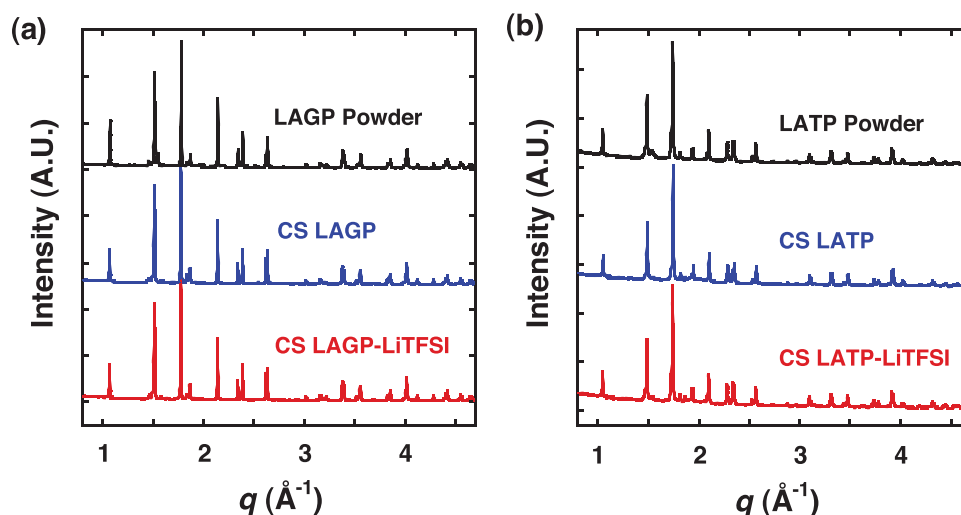


Figure 4. XRD patterns for a) LAGP and b) LATP composite electrolytes. In case of CS LAGP–LiTFSI and CS LATP–LiTFSI, 17 vol% LiTFSI was incorporated.

Table 1. Unit cell parameters and amount of impurity phases.

Process	$a_{\text{hex}}^{\text{a}}$ [\AA^{-1}]	$c_{\text{hex}}^{\text{a}}$ [\AA^{-1}]	AlPO_4^{a} [wt%]	GeO_2^{a} [wt%]	TiO_2^{a} [wt%]
LAGP powder	8.279	20.500	5.3	1.6	–
CS LAGP	8.282	20.488	6.2	1.1	–
CS LAGP–LiTFSI ^b	8.283	20.480	8.4	1.6	–
LATP powder	8.497	20.804	–	–	5.1
CS LATP	8.499	20.807	1.0	–	6.2
CS LATP–LiTFSI ^b	8.499	20.799	2.3	–	5.7

^a) Analyzed using MDI JADE 2010 software; ^b) 17 vol% LiTFSI was incorporated.

$\nu_{(\text{s})}\text{SNS}$ peak at 774.0 cm^{-1} from pure LiTFSI was shifted to 766.7 cm^{-1} . This shift is due to hydrogen bonding from solvation of TFSI^- by water. As the concentration of LiTFSI in water increases, this peak shifts to higher wavenumbers, up to 769.7 cm^{-1} , and saturates at concentrations of about 20 M. We hypothesize that at this concentration, contact ion pairs are formed.^[31,32] The $\nu_{(\text{s})}\text{SNS}$ peak of CS LAGP–LiTFSI (770.2 cm^{-1}) is close to what is observed in 20 M LiTFSI in water, but slightly more shifted toward pure LiTFSI. The same behavior was observed in the $\nu_{(\text{as})}\text{SNS}$ and $\delta_{(\text{s})}\text{CF}_3$ peaks (Figure 5b,c). The $\delta_{(\text{s})}\text{CF}_3$ peak in CS LAGP–LiTFSI is shifted to a higher wavenumber than that of pure LiTFSI because LAGP restricts the movement of Li^+ , thereby promoting a stronger contact ion pair between Li^+ and TFSI^- that influences the $\delta_{(\text{s})}\text{CF}_3$ mode. FT-IR spectra suggest that LiTFSI in CS LAGP–LiTFSI is localized along grain boundaries where the Li^+ and TFSI^- ions are strongly associated, but with small amount of water molecules present. Thus, we speculate that LiTFSI in CS LAGP–LiTFSI is similar to the “water-in-salt” electrolyte system previously developed.^[33,34] The strong association of water to salt molecules in highly concentrated electrolytes enables stable and high-voltage Li-ion batteries due to the scarcity of free water molecules.^[33] Thus, in our composites, this “water-in-salt” aids in Li-ion transport through grain boundaries.

Electrochemical performance of CS LAGP–LiTFSI was examined in Li metal/CS LAGP–LiTFSI/Li metal symmetric

cells to probe the stability of the composite. As shown in Figure S8a (Supporting Information), in accordance with previous reports,^[11,35,36] a large total resistance was observed due to high interfacial resistances between Li metal and CS LAGP–LiTFSI. As shown in Figure S8b (Supporting Information), symmetric cells did not show stable cycling behavior, but instead large increases in the voltage due to the induction of high interfacial resistances and Ge reduction of LAGP by Li metal.^[36] To reduce interfacial resistances, we added a small amount of liquid electrolyte (4 M lithium bis(fluorosulfonyl) imide salt (LiFSI) in 1,2-dimethoxyethane (DME) ($\approx 5.0\text{ }\mu\text{L cm}^{-2}$) at the electrode contacts, as has been demonstrated previously to promote stable Li plating/stripping with high Coulombic efficiency (CE).^[6] A small amount of liquid electrolyte produces a solid–liquid electrolyte interphase that can prevent the reduction of Ge of LAGP by Li metal.^[37] Figure S9 (Supporting Information) shows that liquid electrolytes (4 M LiFSI) only wet the surface of CS LAGP–LiTFSI and do not infiltrate into pellets. As shown in Figure 6a, total resistances were dramatically reduced from about 7500 to 1300 $\Omega\text{ cm}^2$ with the addition of liquid electrolyte, from an increase in the effective contact area and from reduction of unwanted interfacial reactions. Two semicircles were observed in the Nyquist plot of symmetric cells, where a semicircle in the medium-frequency range can be attributed to Li-ion conduction at grain boundaries, and another at low frequency is due to interfacial

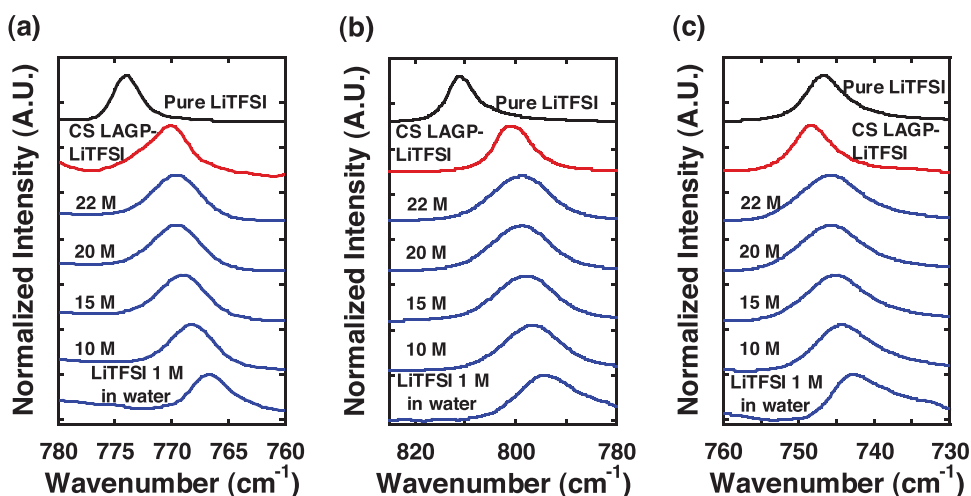


Figure 5. FT-IR spectra of CS LAGP–LiTFSI (25 vol%), pure LiTFSI, and LiTFSI solution in DI water with different concentrations. a) SNS symmetric stretch ($\nu_{(\text{s})}\text{SNS}$), b) SNS asymmetric stretch ($\nu_{(\text{as})}\text{SNS}$), and c) in-plane symmetric deformation of CF_3 ($\delta_{(\text{s})}\text{CF}_3$) from LiTFSI.

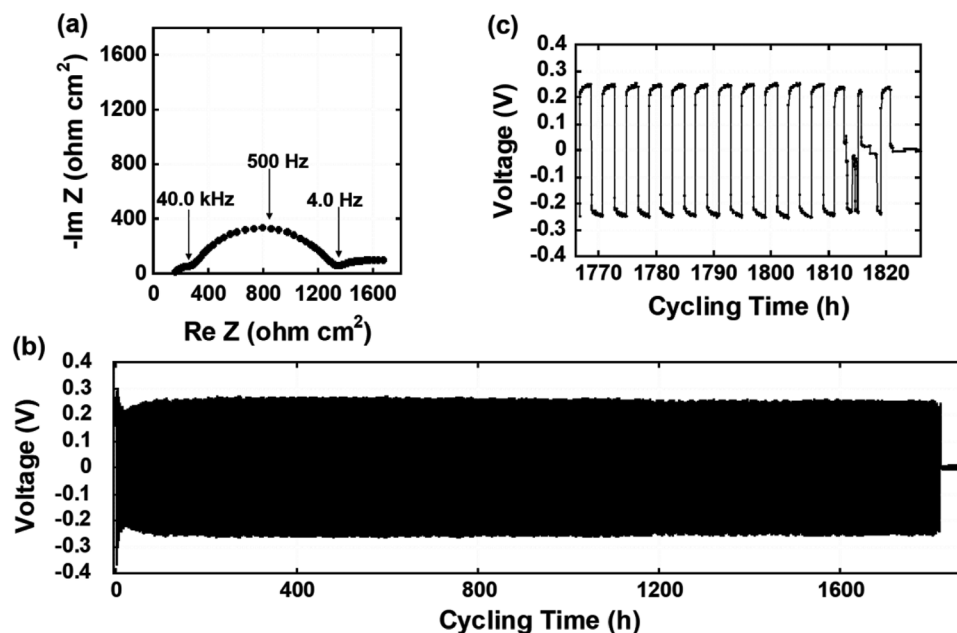


Figure 6. a) Nyquist plot for Li/CS LAGP–LiTFSI (17 vol%)/Li symmetric cells. b) Voltage profile of the Li plating/stripping test at 0.2 mAh cm^{-2} . c) Last few cycles of the Li plating/stripping test.

resistances (Figure 6a). Detailed analysis for determining grain boundary resistances of CS LAGP–LiTFSI and interfacial resistance in symmetric cells through an equivalent circuit is shown in Figure S10 (Supporting Information).^[38] Figure 6b displays plating–stripping tests of symmetric cells at 0.2 mAh cm^{-2} (0.1 mA cm^{-2} for 2 h), and the last cycles are presented in Figure 6c. The voltage profiles exhibited stable cycling over 1800 h without any voltage drop or signatures of Li dendrite growth. The voltage profile becomes unstable around 1810 h, followed by a sudden drop of the voltage to 0 V at 1821 h due to short-circuiting (Figure 6c). Nevertheless, our ceramic–salt electrolytes demonstrate the stability needed for incorporation in all-solid-state Li metal batteries.

3. Conclusions

We have developed ceramic–salt composite electrolytes by cold sintering at $130 \text{ }^\circ\text{C}$, thereby effectively bridging the gap in processing temperature between organic salts and ceramic materials. The use of a LiTFSI aqueous solution for cold sintering is a simple yet effective way to produce composite electrolytes with high relative densities. As model systems, we prepared cold sintered composites of LAGP or LATP with LiTFSI that exhibit ionic conductivities of $2.3 \times 10^{-4} \text{ S cm}^{-1}$ at room temperature and similar activation energies as that of LAGP and LATP sintered above $800 \text{ }^\circ\text{C}$. Stable cycling over 1800 h at 0.2 mAh cm^{-2} of LAGP–LiTFSI composites in Li metal symmetric cells was also demonstrated. Cold sintering enables synthesis of ceramic–salt composites that have significant potential in a wide variety of applications, such as solid electrolytes, composites cathodes, or as multifunctional or responsive structural materials.

4. Experimental Section

Materials: LAGP powder with a volume mean diameter of particles M_v of $26.13 \text{ }\mu\text{m}$ and LATP powder ($\text{Li}_2\text{O–Al}_2\text{O}_3\text{–SiO}_2\text{–P}_2\text{O}_5\text{–TiO}_2$ with 5.7 wt% of Li_2O , 8.0 wt% of Al_2O_3 , 2.7 wt% of SiO_2 , 52.4 wt% of P_2O_5 , and 32.2 wt% of TiO_2 , and crystalline phase of $\text{Li}_{1+x}\text{Al}_x\text{Ti}_{2-x}\text{Si}_y\text{P}_{3-y}\text{O}_{12}$ ^[26,27]) with an M_v of $1.15 \text{ }\mu\text{m}$ were purchased from Toshiba Manufacturing Co. and Ohara Inc., respectively. LATP films (LICGC SP-01, 19 mm diameter \times $160 \text{ }\mu\text{m}$ thickness) were purchased from Ohara Inc. LiTFSI and LiFSI were purchased from Sigma Aldrich and TCI America, respectively. Lithium chips (16 mm diameter \times $250 \text{ }\mu\text{m}$ thickness) were purchased from MTI Corporation. All of the materials were used without further treatment or purification.

Preparation of Ceramic–Salt Composite Electrolytes from Cold Sintering: 10 wt% of DI water was added to LAGP powder and homogeneously mixed in a mortar and pestle. For CS LAGP–LiTFSI, LiTFSI was first dissolved in DI water at 0.63–3.5 M concentration, and the solution was then mixed with LAGP powder. The moistened powder was placed in a pellet die to apply 380 MPa of uniaxial pressure at $130 \text{ }^\circ\text{C}$ for 2 h using a Carver press. To maintain a uniform temperature, the press plates were heated and the pellet die was covered by a band heater. The pressed pellets were then polished by 400, 800, and 2500 grit sandpaper, which led to uniform and mirror-like surfaces. For the preparation of CS LATP–LiTFSI, all processes were the same, except that 20 wt% DI water was mixed with powders and 620 MPa uniaxial pressure was applied. For comparison, S LAGP was also prepared by heating LAGP powder at $825 \text{ }^\circ\text{C}$ for 10 h in a furnace according to previous reports.^[15,17] The prepared electrolytes were round in shape with a thickness of about 1.0 mm and a diameter of about 12.7 mm. Volume percent of LiTFSI relative to LAGP or LATP was obtained from weight percent of LiTFSI by taking theoretical densities of LiTFSI (1.33 g cm^{-3}) and LAGP (3.43 g cm^{-3}) and bulk density of Ohara LATP films (2.72 g cm^{-3}). Because of the low volatility of LiTFSI, it was assumed that all of LiTFSI in solution was incorporated into ceramic electrolytes when cold sintered.

Characterization: Relative densities of electrolytes of CS LAGP–LiTFSI and CS LATP–LiTFSI were calculated by taking the ratio of measured densities to theoretical density of LAGP (3.43 g cm^{-3}) and bulk density of Ohara LATP films (2.72 g cm^{-3}), respectively.^[39] Experimental densities

were obtained by measuring weight and volume. Ionic conductivities were extracted from Nyquist plots measured using a Solartron Ametek Modulab with an AC amplitude of 10 mV in the range of 10^{-1} – 10^6 Hz. As electrodes, 100 nm Au was sputtered on both sides of ceramic or composite pellets. Measurements were performed from 0 to 100 °C. Microstructures of fracture surfaces of electrolytes were obtained by a field emission scanning electron microscope (FESEM, NanoSEM 630). Crystal structures and phase purity were determined by X-ray diffraction (PANalytical Empyrean XRD system) with Cu K α radiation in the 2θ range of 10° – 70° . The crystal structures and weight percentages of impurity phases were analyzed by fitting peaks using MDI JADE 2010 software. FT-IR spectra were obtained using a Bruker Vertex 70 FT-IR spectrometer (Bruker, Billerica, MA) with a mercury–cadmium telluride detector. The spectra were collected with a ZnSe crystal at a spectral resolution of 2 cm^{-1} and 500 scans. The symmetric coin cells of Li/CS LAGP–LiTFSI/Li were assembled in an argon-filled glovebox. CS LAGP–LiTFSI electrolytes were polished to a thickness of about 400 μm . To reduce the resistance of solid–solid interface, 4 M LiFSI solution in DME ($5.0\ \mu\text{L cm}^{-2}$) was added in between Li metal and electrolytes. Resistances of grains, grain boundaries, and interfaces in the symmetric coin cells were obtained by fitting Nyquist plots using an equivalent circuit model. The galvanostatic Li $^+$ charge and discharge measurements of Li/LAGP–LiTFSI/Li cells were measured using a Neware Battery Testing System BTS3000 at 20 °C.

Supporting Information

Supporting Information is available from the Wiley Online Library or from the author.

Acknowledgements

Financial support was acknowledged from the Advanced Research Projects Agency-Energy (ARPA-E), U.S. Department of Energy, under Award Number DE-AR0000766.

Conflict of Interest

The authors declare no conflict of interest.

Keywords

all solid state Li metal batteries, ceramic electrolytes, composite electrolytes, ionic conductivity, low temperature sintering

Received: November 6, 2018

Revised: March 2, 2019

Published online:

- [1] N. Nitta, F. Wu, J. T. Lee, G. Yushin, *Mater. Today* **2015**, *18*, 252.
 [2] a) X.-B. Cheng, R. Zhang, C.-Z. Zhao, Q. Zhang, *Chem. Rev.* **2017**, *117*, 10403; b) P. Albertus, S. Babinec, S. Litzelman, A. Newman, *Nat. Energy* **2018**, *3*, 16.
 [3] Y. Chunpeng, F. Kun, Z. Ying, H. Emily, H. Liangbing, *Adv. Mater.* **2017**, *29*, 1701169.
 [4] F. Lei, W. Shuya, L. Siyuan, L. Qi, L. Yingying, *Adv. Energy Mater.* **2018**, *8*, 1702657.
 [5] M. D. Tikekar, S. Choudhury, Z. Tu, L. A. Archer, *Nat. Energy* **2016**, *1*, 16114.

- [6] J. Qian, W. A. Henderson, W. Xu, P. Bhattacharya, M. Engelhard, O. Borodin, J.-G. Zhang, *Nat. Commun.* **2015**, *6*, 6362.
 [7] a) F. Ding, W. Xu, X. Chen, J. Zhang, M. H. Engelhard, Y. Zhang, B. R. Johnson, J. V. Crum, T. A. Blake, X. Liu, J.-G. Zhang, *J. Electrochem. Soc.* **2013**, *160*, A1894; b) F. Ding, W. Xu, G. L. Graff, J. Zhang, M. L. Sushko, X. Chen, Y. Shao, M. H. Engelhard, Z. Nie, J. Xiao, X. Liu, P. V. Sushko, J. Liu, J.-G. Zhang, *J. Am. Chem. Soc.* **2013**, *135*, 4450.
 [8] A. Manthiram, X. Yu, S. Wang, *Nat. Rev. Mater.* **2017**, *2*, 16103.
 [9] M. Ramaswamy, T. Venkataraman, W. Werner, *Angew. Chem., Int. Ed.* **2007**, *46*, 7778.
 [10] a) A. Sharafi, C. G. Haslam, R. D. Kerns, J. Wolfenstine, J. Sakamoto, *J. Mater. Chem. A* **2017**, *5*, 21491; b) K. Fu, Y. Gong, G. T. Hitz, D. W. McOwen, Y. Li, S. Xu, Y. Wen, L. Zhang, C. Wang, G. Pastel, J. Dai, B. Liu, H. Xie, Y. Yao, E. D. Wachsman, L. Hu, *Energy Environ. Sci.* **2017**, *10*, 1568; c) Y. Li, W. Zhou, X. Chen, X. Lü, Z. Cui, S. Xin, L. Xue, Q. Jia, J. B. Goodenough, *Proc. Natl. Acad. Sci. USA* **2016**, *113*, 13313.
 [11] W. Zhou, S. Wang, Y. Li, S. Xin, A. Manthiram, J. B. Goodenough, *J. Am. Chem. Soc.* **2016**, *138*, 9385.
 [12] J. Fu, *Solid State Ionics* **1997**, *104*, 191.
 [13] a) H. Kitaura, H. Zhou, *Energy Environ. Sci.* **2012**, *5*, 9077; b) D. Safanama, S. Adams, *J. Power Sources* **2017**, *340*, 294.
 [14] E. Zhao, F. Ma, Y. Guo, Y. Jin, *RSC Adv.* **2016**, *6*, 92579.
 [15] C. R. Mariappan, C. Yada, F. Rosciano, B. Roling, *J. Power Sources* **2011**, *196*, 6456.
 [16] L. Yutao, X. Biyi, X. Henghui, D. Huanan, L. Xujie, X. Sen, Z. Weidong, X. Leigang, F. Gengtao, M. Arumugam, J. B. Goodenough, *Angew. Chem., Int. Ed.* **2017**, *56*, 753.
 [17] H. S. Jadhav, M.-S. Cho, R. S. Kalubarme, J.-S. Lee, K.-N. Jung, K.-H. Shin, C.-J. Park, *J. Power Sources* **2013**, *241*, 502.
 [18] S. S. Berbano, J. Guo, H. Guo, M. T. Lanagan, C. A. Randall, *J. Am. Ceram. Soc.* **2017**, *100*, 2123.
 [19] a) F. Han, J. Yue, C. Chen, N. Zhao, X. Fan, Z. Ma, T. Gao, F. Wang, X. Guo, C. Wang, *Joule* **2018**, *2*, 497; b) S.-D. Lee, K.-N. Jung, H. Kim, H.-S. Shin, S.-W. Song, M.-S. Park, J.-W. Lee, *ChemSusChem* **2017**, *10*, 2175; c) S. Ohta, J. Seki, Y. Yagi, Y. Kihira, T. Tani, T. Asaoka, *J. Power Sources* **2014**, *265*, 40.
 [20] J. Guo, H. Guo, A. L. Baker, M. T. Lanagan, E. R. Kupp, G. L. Messing, C. A. Randall, *Angew. Chem., Int. Ed.* **2016**, *55*, 11457.
 [21] J. Guo, S. S. Berbano, H. Guo, A. L. Baker, M. T. Lanagan, C. A. Randall, *Adv. Funct. Mater.* **2016**, *26*, 7115.
 [22] J.-P. Maria, X. Kang, R. D. Floyd, E. C. Dickey, H. Guo, J. Guo, A. Baker, S. Funihashi, C. A. Randall, *J. Mater. Res.* **2017**, *32*, 3205.
 [23] H. Guo, J. Guo, A. Baker, C. A. Randall, *ACS Appl. Mater. Interfaces* **2016**, *8*, 20909.
 [24] a) M. Kerner, N. Plylahan, J. Scheers, P. Johansson, *Phys. Chem. Chem. Phys.* **2015**, *17*, 19569; b) S. F. Lux, L. Terborg, O. Hachmöller, T. Placke, H.-W. Meyer, S. Passerini, M. Winter, S. Nowak, *J. Electrochem. Soc.* **2013**, *160*, A1694.
 [25] a) Y.-H. Cho, J. Wolfenstine, E. Rangasamy, H. Kim, H. Choe, J. Sakamoto, *J. Mater. Sci.* **2012**, *47*, 5970; b) S. Yu, R. D. Schmidt, R. Garcia-Mendez, E. Herbert, N. J. Dudney, J. B. Wolfenstine, J. Sakamoto, D. J. Siegel, *Chem. Mater.* **2016**, *28*, 197.
 [26] Ohara Inc., Lithium-Ion Conductive Glass-Ceramics, <http://www.ohara-inc.co.jp/en/product/electronics/licgscsp01.html> (accessed: February 2019).
 [27] K. Osaga (Ohara Inc.), *US 2012/0237834 A1*, **2012**.
 [28] X. Xu, Z. Wen, X. Wu, X. Yang, Z. Gu, *J. Am. Ceram. Soc.* **2007**, *90*, 2802.
 [29] a) L. Huang, Z. Wen, M. Wu, X. Wu, Y. Liu, X. Wang, *J. Power Sources* **2011**, *196*, 6943; b) M. Pérez-Estébanez, J. Isasi-Marín, D. M. Többsen, A. Rivera-Calzada, C. León, *Solid State Ionics* **2014**, *266*, 1.

- [30] a) N. V. Kosova, E. T. Devyatkina, A. P. Stepanov, A. L. Buzlukov, *Ionics* **2008**, *14*, 303; b) C. Drouet, *Biomed Res. Int.* **2013**, *2013*, 1.
- [31] Z. Wang, W. Gao, X. Huang, Y. Mo, L. Chen, *J. Raman Spectrosc.* **2001**, *32*, 900.
- [32] D. M. Seo, O. Borodin, S.-D. Han, P. D. Boyle, W. A. Henderson, *J. Electrochem. Soc.* **2012**, *159*, A1489.
- [33] L. Suo, O. Borodin, T. Gao, M. Olguin, J. Ho, X. Fan, C. Luo, C. Wang, K. Xu, *Science* **2015**, *350*, 938.
- [34] L. Suo, O. Borodin, W. Sun, X. Fan, C. Yang, F. Wang, T. Gao, Z. Ma, M. Schroeder, A. von Cresce, S. M. Russell, M. Armand, A. Angell, K. Xu, C. Wang, *Angew. Chem., Int. Ed.* **2016**, *55*, 7136.
- [35] C.-L. Tsai, V. Roddatis, C. V. Chandran, Q. Ma, S. Uhlenbruck, M. Bram, P. Heitjans, O. Guillon, *ACS Appl. Mater. Interfaces* **2016**, *8*, 10617.
- [36] H. Chung, B. Kang, *Chem. Mater.* **2017**, *29*, 8611.
- [37] C. Wang, Q. Sun, Y. Liu, Y. Zhao, X. Li, X. Lin, M. N. Banis, M. Li, W. Li, K. R. Adair, D. Wang, J. Liang, R. Li, L. Zhang, R. Yang, S. Lu, X. Sun, *Nano Energy* **2018**, *48*, 35.
- [38] Y. Leng, S. Ge, D. Marple, X.-G. Yang, C. Bauer, P. Lamp, C.-Y. Wang, *J. Electrochem. Soc.* **2017**, *164*, A1037.
- [39] J. Yang, Z. Huang, B. Huang, J. Zhou, X. Xu, *Solid State Ionics* **2015**, *270*, 61.